



Highly Sensitive Pseudocapacitive Iontronic Pressure Sensor with Broad Sensing Range

Cite as

Nano-Micro Lett.

(2021) 13:140

Libo Gao^{1,2} ✉, Meng Wang^{1,2}, Weidong Wang^{1,2} ✉, Hongcheng Xu^{1,2}, Yuejiao Wang³, Haitao Zhao⁴, Ke Cao^{1,2}, Dandan Xu^{1,2}, Lei Li⁵ ✉

Received: 5 March 2021

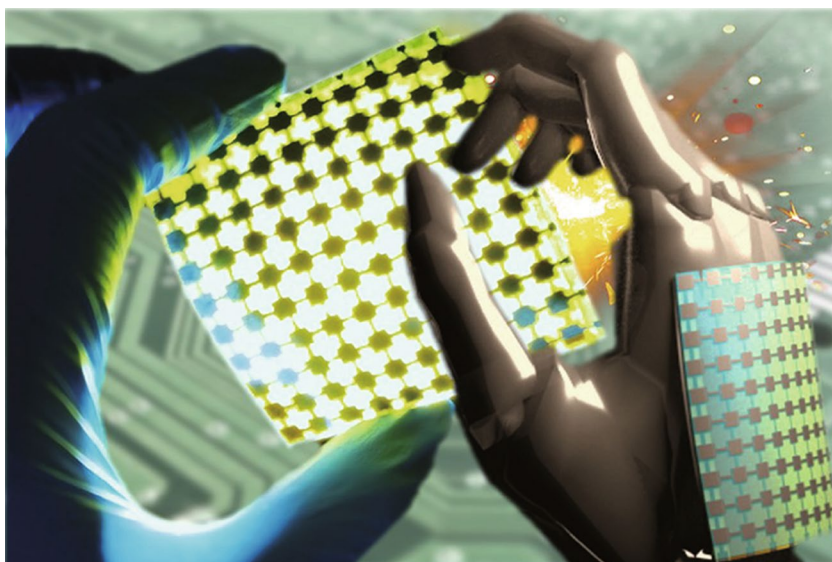
Accepted: 11 May 2021

© The Author(s) 2021

HIGHLIGHTS

- The iontronic pressure sensor achieved an ultrahigh sensitivity ($S_{\min} > 200 \text{ kPa}^{-1}$, $S_{\max} > 45,000 \text{ kPa}^{-1}$).
- The iontronic pressure sensor exhibited a broad sensing range of over 1.4 MPa.
- Pseudocapacitive iontronic pressure sensor using MXene was proposed.

ABSTRACT Flexible pressure sensors are unprecedentedly studied on monitoring human physical activities and robotics. Simultaneously, improving the response sensitivity and sensing range of flexible pressure sensors is a great challenge, which hinders the devices' practical application. Targeting this obstacle, we developed a $\text{Ti}_3\text{C}_2\text{T}_x$ -derived iontronic pressure sensor (TIPS) by taking the advantages of the high intercalation pseudocapacitance under high pressure and rationally designed structural configuration. TIPS achieved an ultrahigh sensitivity ($S_{\min} > 200 \text{ kPa}^{-1}$, $S_{\max} > 45,000 \text{ kPa}^{-1}$) in a broad sensing range of over 1.4 MPa and low limit of detection of 20 Pa as well as stable long-term working durability for 10,000 cycles.



The practical application of TIPS in physical activity monitoring and flexible robot manifested its versatile potential. This study provides a demonstration for exploring pseudocapacitive materials for building flexible iontronic sensors with ultrahigh sensitivity and sensing range to advance the development of high-performance wearable electronics.

KEYWORDS Iontronic sensor; Flexible electronics; Pressure sensor; Pseudocapacitance; $\text{Ti}_3\text{C}_2\text{T}_x$ MXene

✉ Libo Gao, lbgao@xidian.edu.cn; Weidong Wang, wangwd@mail.xidian.edu.cn; Lei Li, l-li@xjtu.edu.cn

¹ School of Mechano-Electronic Engineering, Xidian University, Xian 710071, Shaanxi, P. R. China

² CityU-Xidian Joint Laboratory of Micro/Nano-Manufacturing, Shenzhen 518057, P. R. China

³ Department of Mechanical Engineering, City University of Hong Kong, Kowloon 999077, Hong Kong SAR, P. R. China

⁴ Materials Interfaces Center, Shenzhen Institutes of Advanced Technology, Chinese Academy of Sciences, Shenzhen 518055, Guangdong, P. R. China

⁵ State Key Laboratory for Mechanical Behavior of Materials, Xian Jiaotong University, No. 28, Xianning West Road, Xian 710049, Shaanxi, P. R. China



1 Introduction

The booming development of human–machine interaction (HMI), 5G communication, robotics, wearable electronics and Internet of things (IoTs) has greatly stimulated the demand for wearable sensors [1–10]. Among them, the flexible pressure sensor with high sensitivity and broad sensing range is highly pursued for their good sensing performance to mechanical stimuli along with their ability to be stretched, bent, or twisted into any format under various application scenarios [11–17]. The pressure sensors typically can be classified into four types of piezoresistive, piezocapacitive, piezoelectric, and triboelectricity based on their sensing mechanisms. Piezocapacitive pressure sensor (PPS) has attracted considerable attention due to their merits of simple configuration, low power consumption and favorable working stability [11, 18]. Until now most of the reports so far have demonstrated limited performance, especially the sensitivity (below 10 kPa^{-1}) and sensing range (below 1 MPa) [19–21]. Therefore, improving the sensitivity and sensing range of PPS is necessary to further extend the reach of existing applications.

Several strategies were developed to improve the sensitivity and sensing range of the PPS, such as (a) building microstructures on electrode or dielectric; (b) using a composite dielectric; (c) engineering holes inside the dielectric layer [22]. Engineering microstructure of the electrode or dielectric is widely used. For instance, Guo et al. achieved a graded intrafillable architecture-based iontronic PPS with unprecedentedly high sensitivity ($S_{\min} > 220 \text{ kPa}^{-1}$) and a broad pressure regime (0.08 Pa–360 kPa) [23]. Kim et al. developed the top floating electrode for iontronic PPS with greatly enhanced sensitivity [20]. Additionally, recently introducing the remarkable interfacial capacitance for PPS by electrical double layer (EDL) effect is also an effective strategy [24]. For example, Pan et al. introduced the iontronic PPS based on the EDL capacitive materials [21, 25, 26], such as graphene [20], silver [21], and Au [23]. Thanks to its high areal capacitance (up to nF or even near μF), the EDL-based iontronic sensor showed much higher sensitivity and broader sensing range than traditional PPS. While both of these two strategies have been greatly improved the devices' sensitivity and sensing range, there is still plenty of room for performance improvement. For example, the idea that using pseudocapacitive electrode materials instead of

EDL materials can enhance the capacitance has already been demonstrated in electrochemical supercapacitor devices [27]. As one might expect, using pseudocapacitive iontronic PPS combined with a novel configuration would enhance the sensitivity and sensing range significantly.

Herein, we developed a $\text{Ti}_3\text{C}_2\text{T}_x$ -derived iontronic pressure sensor (TIPS) with a novel configuration of the top floating electrode along with a microstructured dielectric film. $\text{Ti}_3\text{C}_2\text{T}_x$ has superior electronic conductivity ($\sim 10,000 \text{ S cm}^{-1}$), electrochemical, optical and mechanical properties. It presents a wide range of application in energy storage, sensor, electromagnetic interference and optoelectronics. It was chosen as electrodes of flexible PPS by using its ions intercalation-based pseudocapacitance that significantly exceeds EDL electrodes materials. The floating electrode design along with the microstructured dielectric film further enhanced the sensitivity deeply. Benefited from the synergistic effect between the electrode materials and the device configuration, TIPS exhibited unprecedentedly ultrahigh sensitivity ($S_{\min} > 200 \text{ kPa}^{-1}$, $S_{\max} > 45,000 \text{ kPa}^{-1}$), broad sensing range (20 Pa to 1.4 MPa), low limit of detection (LOD) of 20 Pa as well as stable long-term working durability for 10,000 cycles. The sensors are capable of monitoring the physical activity and flexible robot tactile perception. Additionally, the electrode patterns were fabricated via laser-engraving technologies, indicating the manufacturing scalability. This work developed here shed light on the advance of PPS.

2 Experimental Sections

2.1 Preparation of the MXene ($\text{Ti}_3\text{C}_2\text{T}_x$) Nanosheets Solution

The preparation method is similar to reports elsewhere [28]. $\text{Ti}_3\text{C}_2\text{T}_x$ was prepared by immersing 1 g of Ti_3AlC_2 in 40 mL of a hydrochloric acid solution containing 1.6 g of LiF and 9 M HCl at 35°C for 24 h. In this process, HF selectively etched the aluminum in Ti_3AlC_2 . The obtained multilayer $\text{Ti}_3\text{C}_2\text{T}_x$ suspension was centrifuged at 3500 rpm for 5 min to obtain the precipitate, which was rinsed with deionized water until the pH value of the solution was larger than 6. The precipitate was then dispersed in deionized (DI) water and continuously ultrasonicated for 3 h under the protection atmosphere of argon. Finally, the suspension was centrifuged

at 3500 rpm for 60 min to obtain a dark colloidal $\text{Ti}_3\text{C}_2\text{T}_x$ nanosheets solution.

2.2 Preparation of the $\text{Ti}_3\text{C}_2\text{T}_x$ Electrode

The n-WF was washed with alcohol and DI water for three times, respectively. The dried n-WF was directly immersed into the $\text{Ti}_3\text{C}_2\text{T}_x$ nanosheets solution (5 mg mL^{-1}) for 10 s and pulled out slowly for drying at 50°C . To find the optimal amount of MXene for n-WF, this dip-coating process was repeated for 4 times. A thin gold layer, acting as the current collector, was deposited on the conductive n-WF using the magnetic sputtering for 1 min. The obtained conductive n-WF composite material was carefully laminated on PI/PET or pure PI film. The laser (power: 7 W, speed: 2000 mm min^{-1}) was used to engrave the designed pattern. The designed electrode was obtained on flexible substrate after peeling off the unused part.

2.3 Preparation of the Flexible Sensor

PVA-KOH was chosen as the dielectric membrane in the sensor. The preparation of the PVA-KOH was modified from the reported method reported in our previous studies [29, 30]. PVA-KOH gel electrolyte was directly spin-coated on the abrasive paper (400#) and dried at 50°C for 0.5 h. The flexible and mechanically robust film ($20 \mu\text{m}$) can be easily peeled off from the abrasive paper. The ionic membrane was closely attached to the bottom electrode using a soft Ecoflex silicone film with a cavity as an air spacer. To assemble the device, a PET or PI was used to cover the device by double faced adhesive tape (3 M) to bond them together tightly for testing and application study.

2.4 Structural Characterization

Field emission SEM (FESEM, Quanta 450, 20 kV) and the transmission electron microscope (TEM, JEM 2100F) equipped with energy-dispersive spectroscopy (EDS) were used to characterize the structural and morphology information. X-ray diffractometer (XRD, Bruker, D8 ADVANCE) with $\text{Cu K}\alpha$ radiation ($\lambda = 0.15406 \text{ nm}$) was used to identify the phase structure.

2.5 Mechanical and Electromechanical Characterizations

The mechanical performance of the n-WF and ionic membrane was conducted on a mechanical testing machine (Zhi Qu, 990B) with a pulling speed of 0.5 mm min^{-1} . For each testing condition, 5 samples were repeated, and the final result was obtained by averaging. For the electromechanical characterization, the variable resistance, current and capacitance can be recorded in this process by the electrochemical working station (CHI 760E), LCR impedance analyzer (Tonghui, TH 2827A) and IM3536 LCR meter. The CV curves also were recorded by the electrochemical working station under the applied pressure.

2.6 Application of the Sensor

The customized soft gripper can easily be fabricated by 3D printing method. The flexible sensor was mounted onto the end of the gripper and the gripper was fixed onto a three-axis mobile platform and can move freely. The whole system was controlled through wireless remote-control method, which can be control by a micro controller (STM32), and the corresponding signal was captured by an LCR impedance analyzer.

3 Results and Discussion

3.1 Device Fabrication and Structural Characterization

The traditional parallel-plate capacitive sensor is typically composed of a dielectric layer sandwiched between two conducting electrode plates. Its corresponding capacitance was defined as $C = \epsilon_0 \epsilon_r A/d$, where ϵ_0 and ϵ_r are the permittivity of vacuum and dielectric layer, A is the overlapped area, and d is the distance between the two electrode plates, respectively (Fig. 1a). The measured capacitance value of such type of device is typically in the pF-level, which result in inferior sensitivities and increased difficulties in the subsequent circuit processing of the signal. The iontronic sensor is therefore designed in order to increase its capacitance. The previously reported iontronic sensors were merely adopted to the EDL-based electrode materials, hindering their capacitance (Fig. 1b). Here, for the first

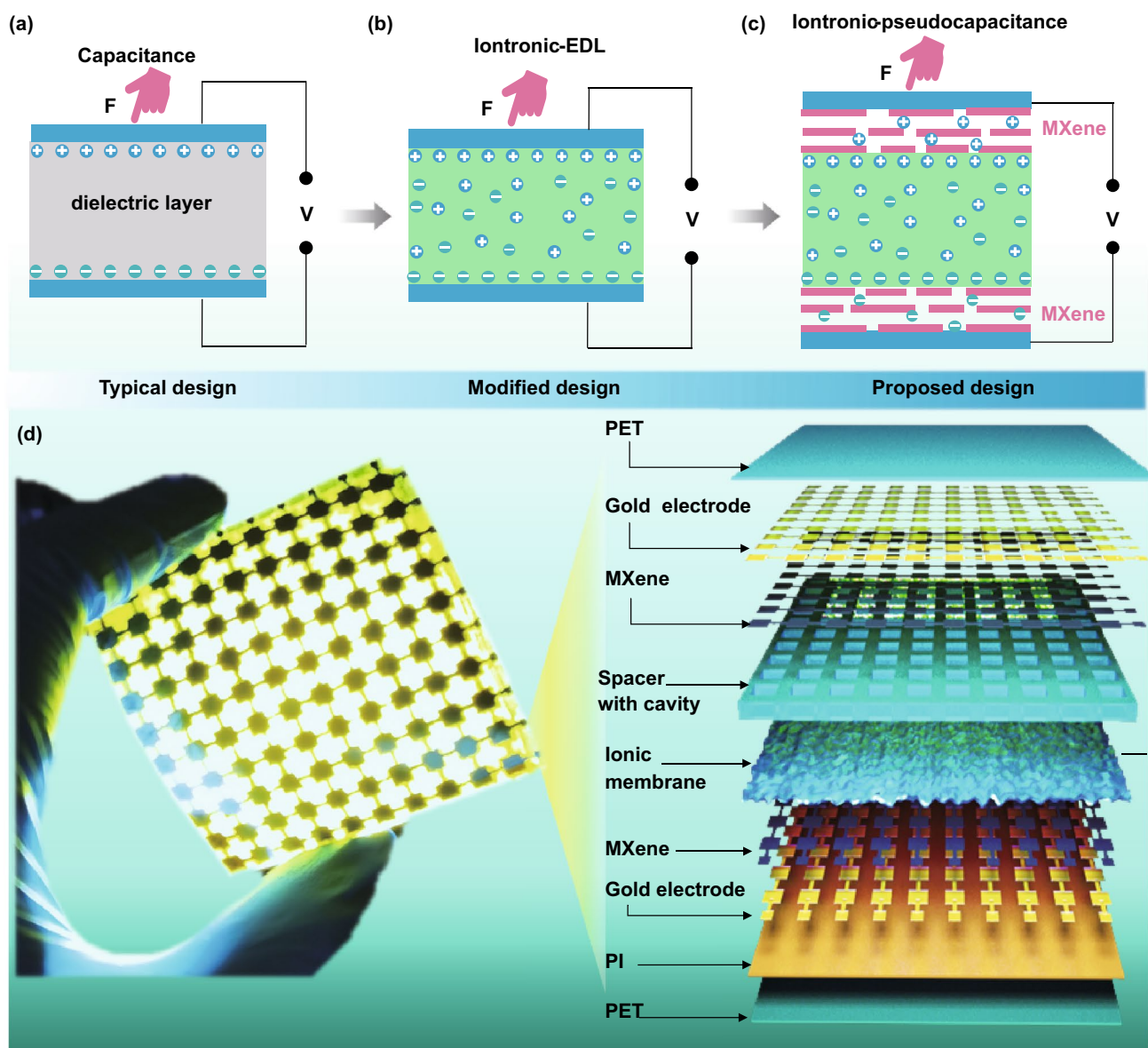


Fig. 1 Flexible TIPS layout and design. Schematic illustration of the mechanism of the **a** traditional PPS, **b** modified design and **c** proposed mechanism of our pseudocapacitance-derived sensors. **d** Digital optical image of the TIPS arrays under bending state and corresponding exploded view layout of the various layers in the sensor

time, MXene was employed as the electrode materials in the iontronic sensor, which has a high capacitance compared to the EDL-based electrode (Fig. 1c) [31, 32]. The contribution of MXene capacitance is primarily derived from the bottom and upper electrode layer by K^+ intercalating into $Ti_3C_2T_x$, resulting in superior sensitivity (S) according to $S = \Delta C/C_0$, where ΔC is the capacitance variation and C_0 is the initial capacitance [33]. Figure 1d shows the as-prepared bendable, flexible sensor array

device, which was mainly composed of $Ti_3C_2T_x$ electrodes coated with the gold layer (current collector), ionic membrane (20 μm) with rough a surface and spacer (500 μm in thickness) with cavity. This rational structure design contributes to a significantly enhance in sensitivity because the initial capacitance is much lower than that under pressure, as direct contact between the upper electrode and the ionic membrane was blocked by the spacer initially. Once the electrode touched the ionic membrane is induced

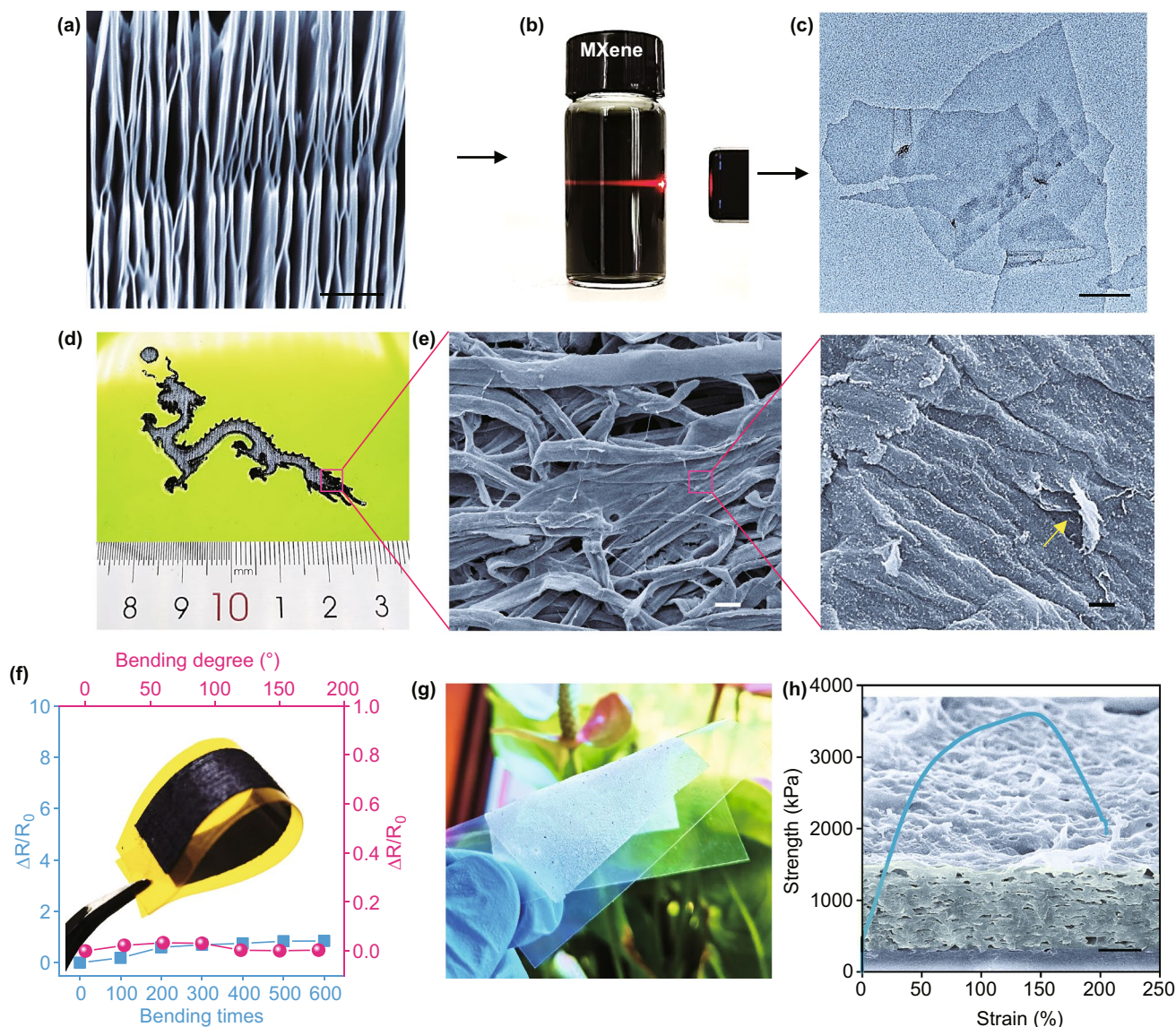


Fig. 2 Structural characterization of the sensing materials and electrode. **a** SEM image of the accordion-microstructured MXene. The scale bar is 500 nm. **b** Tyndall effect of the $\text{Ti}_3\text{C}_2\text{T}_x$ nanosheets solution. **c** TEM image of the $\text{Ti}_3\text{C}_2\text{T}_x$ nanosheets. The scale bar is 100 nm. **d** Laser pattern of a Chinese dragon. **e** SEM image and its corresponding large view of the $\text{Ti}_3\text{C}_2\text{T}_x$ nanosheets coated n-WF. The scale bar is 40 μm and 500 nm, respectively. **f** Bending deformation of the $\text{Ti}_3\text{C}_2\text{T}_x$ electrode and its corresponding resistance change. Inset is the optical image of the $\text{Ti}_3\text{C}_2\text{T}_x$ -coated n-WF. **g** Iontronic film on a bending PET film. **h** Mechanical performance of the PVA-KOH film. Inset is corresponding cross-sectional view of the PVA-KOH film. The scale bar is 10 μm

by the applied pressure, the capacitance would dramatically increase due to the shortened pathway between the electrodes.

To obtain the desired electrode pattern, we directly used the laser to engrave $\text{Ti}_3\text{C}_2\text{T}_x$ composite materials laminated on a polyethylene terephthalate (PET)/polyimide (PI)-laminated film ($\sim 120 \mu\text{m}$). Here, the laser-scribing technique with higher pixel fill factor was used to precisely pattern the

electrode arrays (10×10 in $5 \times 5 \text{ cm}^2$, Fig. S1a and Experimental Sections). On the other hand, the dielectric layer, another core part of capacitive sensor device, played an important role in enhancing the sensitivity, detection limit and sensing range. To further boost the sensor's behavior, geometric microengineering design of the dielectric layer was adopted as it can increase the capacitance variation at a given applied pressure through enhancing the electrode

distance change and effective dielectric constant [34]. In this study, we directly spin-coated polyvinyl alcohol (PVA)-KOH gel on rough abrasive paper as a mold. Then, the translucent and mechanically flexible film can be easily peeled off from the mold (Fig. S1b and Experimental Sections).

To prepare the $\text{Ti}_3\text{C}_2\text{T}_x$ electrode, corresponding $\text{Ti}_3\text{C}_2\text{T}_x$ nanosheets were firstly synthesized by chemically etching the Al elements in Ti_3AlC_2 MAX phase with smooth surfaces and stacked layers (see Experimental Sections and Figs. S2, S3) [31, 35]. Figure 2a shows the accordion-microstructured $\text{Ti}_3\text{C}_2\text{T}_x$. In the X-ray diffraction (XRD) patterns of the as-synthesized product, a strong (002) peak located at 6.8° (corresponding d-spacing is 1.2 nm) demonstrates the successful removal of Ti–Al bond and the formation of $\text{Ti}_3\text{C}_2\text{T}_x$ (Fig. S4) [36]. The typical Tyndall effect further evidenced the highly homogeneous distribution of $\text{Ti}_3\text{C}_2\text{T}_x$ nanosheets in water. This is due to the abundantly existed hydroxide and fluorine groups, which is beneficial to the uniform coating of $\text{Ti}_3\text{C}_2\text{T}_x$ layer on the substrate (Fig. 2b) [37]. The as-obtained $\text{Ti}_3\text{C}_2\text{T}_x$ nanosheets exhibited 2D features with size of 300–500 nm (Fig. 2c). Then, a simple yet effective “dip-coating” strategy was used to fabricate the soft and robust electrode building on the nonwoven fabrics (n-WF). Benefited from the flexibility and high resolution ($\sim 100 \mu\text{m}$) of the laser-scribing strategy, complicated fabrics patterns, such as the Chinese dragon, can be achieved (Fig. 2d). The SEM images suggested the uniform and thin coating of $\text{Ti}_3\text{C}_2\text{T}_x$ nanosheets on the raw n-WF, which possessed a coarse surface formed by intertwined and tangled fibers, along with abundant porosities within the weaved electrode compared to the raw n-WF (Figs. 2e and S5). The geometrical entanglement of the individual fiber contributed to enhance the mechanical performance and conductive stability of the composites. The increased roughness results in a larger accessible surface area and thus improved the electrochemical performance for high specific capacitance accordingly. Additionally, the performances of the composite materials are largely dependent on the dip-coating times. Figure S6a–e shows the morphology of the pristine n-WFs and samples coated for 1–4 times, respectively. With the increased coating times, the sheet resistance decreased from 4.6 to $0.9 \Omega \text{ cm}^{-2}$ (Fig. S6f), yet the $\text{Ti}_3\text{C}_2\text{T}_x$ nanosheets seriously aggregated together when coating reached 4 times; therefore, the n-WF was dip-coated 3 times in the following study. The mechanical performance of the MXene-modified n-WF was also studied and showed a good performance

compared with pure n-WF, with merely a slight mechanical decay (Fig. S7). Specifically, the resistance variation of the composite materials was below 1.5 times below the initial value. It kept stable from 200 to 600 cycles under a bending degree of 90° as the fiber structure reached a stable condition. Similarly, the sample’s conductivity also possessed a steady-state even under bending from 0 to 180° (Fig. 2f).

Additionally, as shown in Figs. S8 and 2g, h, the translucent ionic film maintained a structural integrity under bending deformation on a flexible PET substrate and has successfully replicated the random rough microstructures of the abrasive paper, which increased the sensitivity of the sensor in this study for the following reasons. Firstly, the permittivity of dielectric layer changes when the sensor is compressed, because the displaced volume is air, in which the permittivity is usually lower than that of elastomers [23]. Secondly, the distance between the electrode and the ion membrane reduces greatly, leading to a shortened charge transfer distance, whereas the contact area increased for promoting electrochemical reactions; both contribute in improving the capacitance. Moreover, the tensile test of the film demonstrated an excellent stretchability as large as 150% and fracture strength of 3.5 MPa, which is necessary for building the flexible electronics.

3.2 Device Characterization

The sensitivity, LOD, pressure sensing range, response and relaxation time and the long-term durability are studied to evaluate the sensor’s performance. Figure 3a shows a digital optical image of a single sensor. Figure 3b shows the normalized capacitance variation of the sensors under different pressures. The TIPS showed an ultrahigh sensitivity in a broader pressure sensing range compared to the traditional ones. It had a high sensitivity up to $46,730 \text{ kPa}^{-1}$ within the pressure range of 200–800 kPa, which is much higher than the control sensors of MXene-PDMS, Metal-ionic-based counterparts, and even the TIPS without the spacer (Fig. S9). At high-pressure regime, TIPS still showed superior sensitivity of $17,148 \text{ kPa}^{-1}$ up to 1.4 MPa. Even at relatively low-pressure range, the sensor exhibited outstanding sensitivities over 200 and 5000 kPa^{-1} in the range below 60 and 200 kPa, respectively (Fig. 3c). These results are almost the best one among the reported sensitivity, with the broadest sensing range for the flexible capacitive sensor (Table S1).

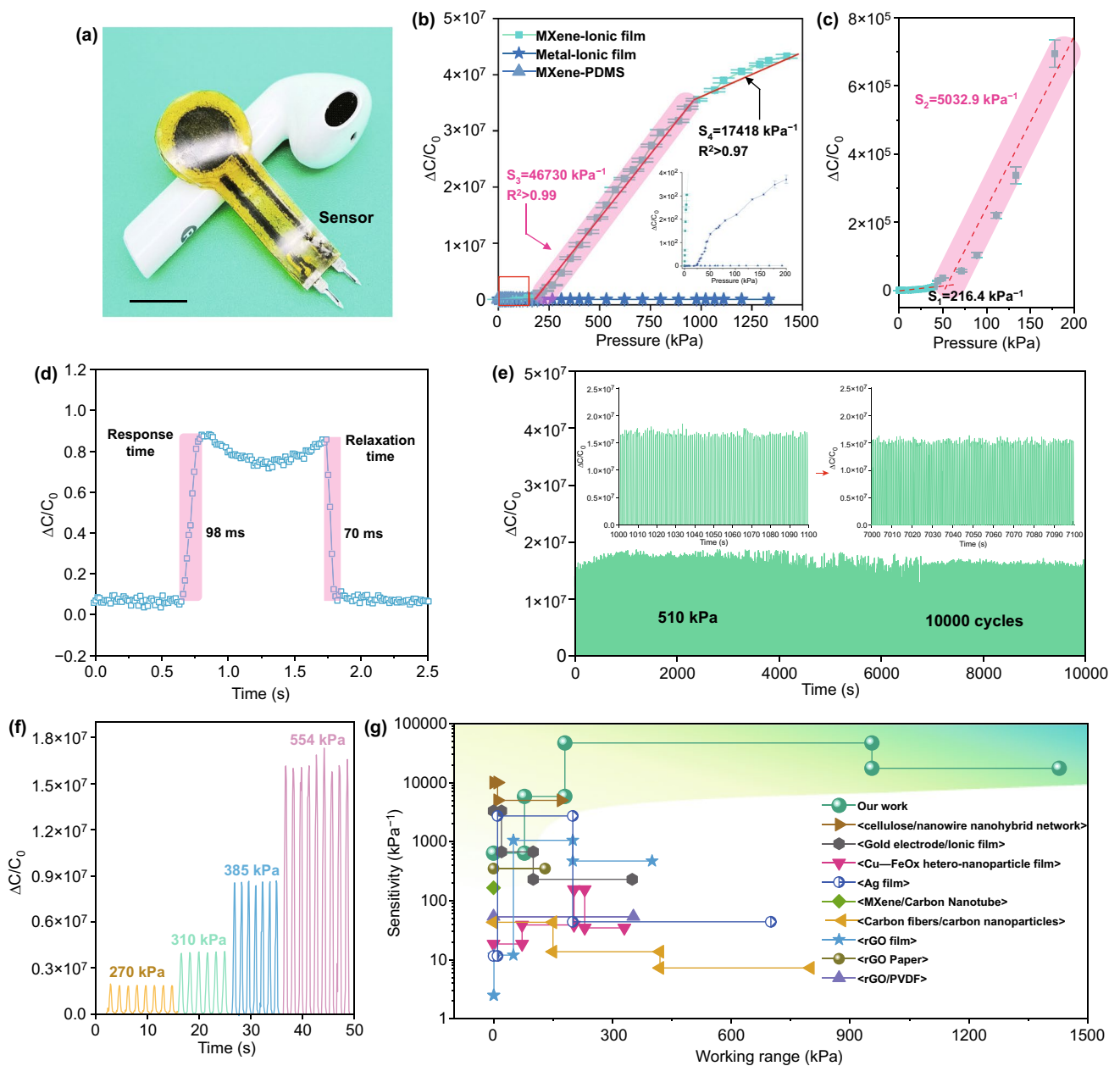


Fig. 3 Characterization of the sensor. **a** Digital optical image of the single sensor device. **b** Capacitance variation versus the pressure change of the sensing materials and **c** its corresponding large view. **d** Response and relaxation time of the flexible sensor. **e** Long-time durability of the sensor under 510 kPa. **f** Capacitance variation of the sensor under various pressure. **g** Comparison of our sensor's sensitivity and sensing range with other reported work

The response time and relaxation time of TIPS are only 98 and 70 ms, respectively, demonstrating that the device responds quickly to the external pressure (Fig. 3d). The long-term durability test of TIPS was studied under pressure of 510 kPa (Fig. 3e). A robust signal output without any decay was observed during 10,000 cycles. It is ascribed to the

electromechanical robustness of the n-WF MXene electrode and ionic membrane of the sensor (Fig. 2f–h). The electromechanical behaviors of TIPS under various dynamic pressures (270, 310, 285 and 554 kPa) were studied. It showed a stable and proportional electrical signal at different pressures (Fig. 3f). The LOD for the sensor is only 20 Pa, indicating

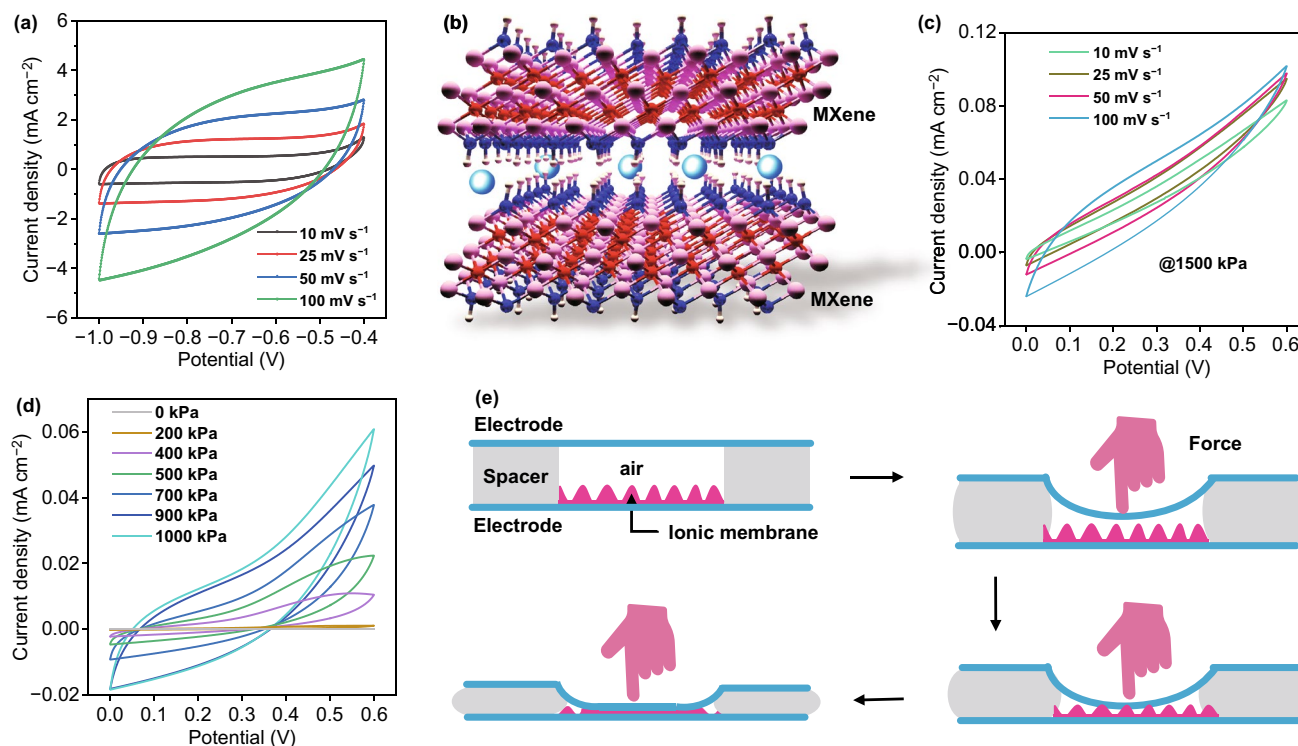


Fig. 4 Mechanism of the iontronic sensor. **a** CV curves of the MXene tested in three-electrode mode in KOH solution. **b** Intercalation of K^+ between $Ti_3C_2T_x$ layers **c** CV curves of the symmetrical configuration of the MXene electrode materials tested in two-electrode mode at various scan rates under applied pressure of 1500 kPa. **d** CV curves of the symmetrical configuration of the MXene electrode materials tested in two-electrode mode at various applied pressures. **e** Schematic illustration of the working mechanism of the iontronic sensor

the great sensitivity to the tiny force (Fig. S10). Figure 3g shows the sensitivity of the sensor relative to the reported works. The developed sensor not only showed an ultrahigh sensitivity, but also an incomparably broad pressure sensing range up to 1.4 MPa. Its performance is superior to the existing pressure sensors [23, 38–45]. To sum up, the iontronic sensor presents superior sensitivity, sensing range, LOD, response/relaxation time when compared to other similar iontronic works (Table S1).

To gain further insight into $Ti_3C_2T_x$ capacitive behavior and elucidate its sensing mechanism, electrochemical evaluations based on both three-electrode system and two-electrode system were carried out. As shown in Fig. 4a, the rectangular shape of the cyclic voltammetry (CV) curves of $Ti_3C_2T_x$ appeared in a three-electrode system in the 2 M KOH electrolyte, demonstrating the typical capacitive behavior through the intercalation of K^+ and H_2O molecules between the $Ti_3C_2T_x$ layers (Fig. 4b) [33, 46, 47]. Considering that the iontronic sensor can also be regarded as the symmetrical supercapacitor device under

the applied pressure, its performance in the two-electrode system was also studied. There was no obvious sluggish observed in the curves, further illustrating the capacitive behaviors of the sensor at various scan rates from 10 to 100 $mV s^{-1}$ under 1500 kPa (Fig. 4c). The shape of the device CV curves would be changed under different pressure since increasing applied pressure would result in capacitance enhancement (Fig. 4d). As expected, the profile of the device CV changed accordingly to the variation of applied pressure from unloaded state of 0 to 1000 kPa. It should be mentioned that the capacitance is too low to be exhibited at CV curves under its original state due to the isolation of the electrode and ionic membrane (Fig. S11a) [21]. The CV curves under various applied pressures from 200 to 1000 kPa exhibited different integrated areas; it is because that with higher pressure, it is more likely to enable improved access areas and short transportation pathway to deep trap sites induced by larger contact areas. The integrated area showed almost linear behaviors, which are in accordance with the results above (Fig. S11b). Based on the

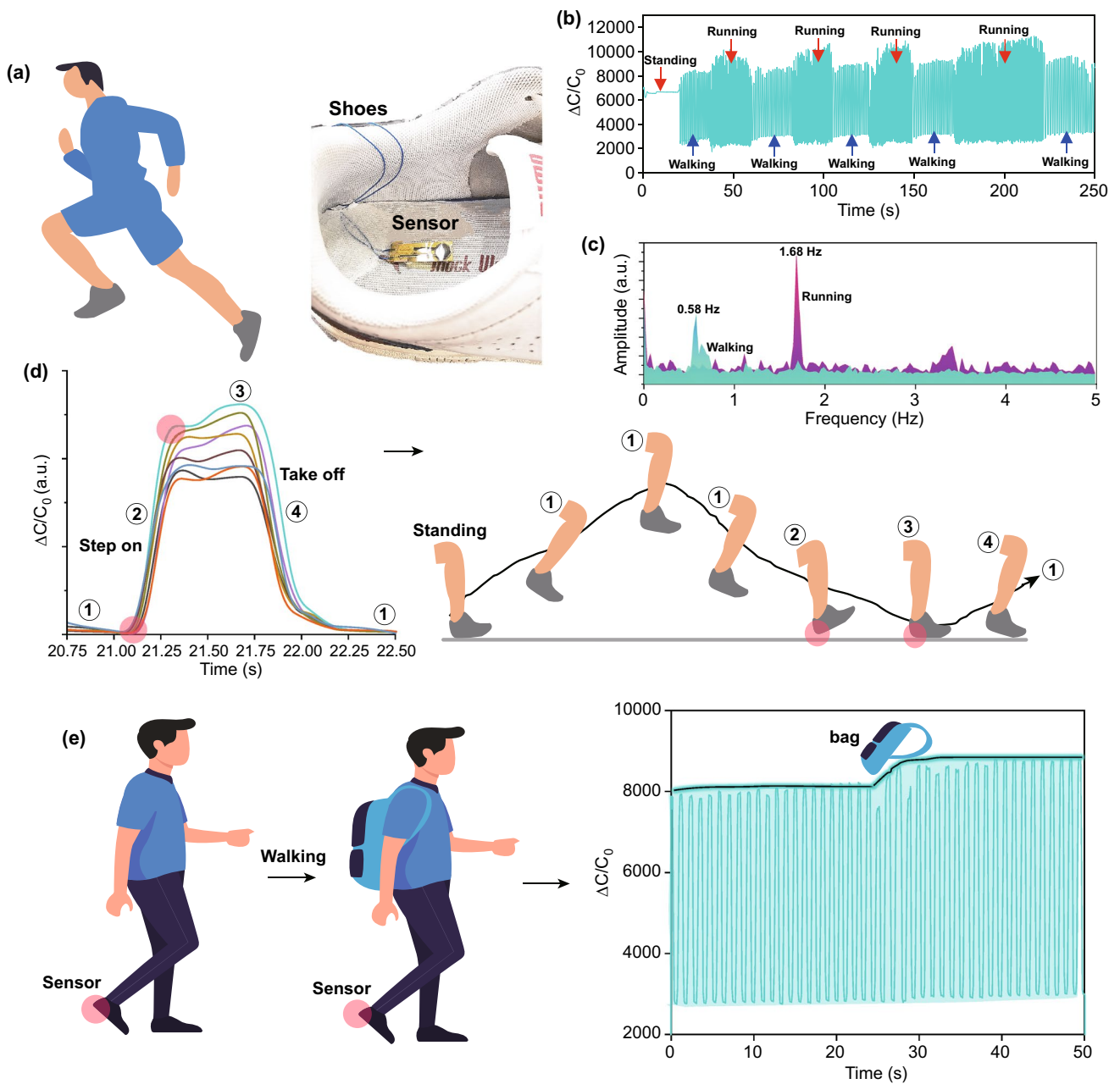


Fig. 5 Practical application of the flexible iontronic sensor on monitoring of physical activity. **a** Optical image of the sensor mounted into the shoes to monitor the physical activity. **b** Physical activity such as standing, walking and running were monitored by the sensor. **c** The FFT spectrum of the walking and running obtained from (b). **d** Walking state was analyzed by the flexible sensor. **e** Sensor’s sensitivity on monitoring the walking statuses with different bearing load

above discussion, the sensing process is mainly composed of the following stages (Fig. 4e). Initially, TIPS worked as a normal PPS with a low capacitance due to the separation of $Ti_3C_2T_x$ electrodes and ionic membrane caused by the air spacer. With the increased applied pressure, the

capacitance increases due to the reduced distance between two electrodes. Once the applied pressure increased to a state where the upper electrode and ionic membrane were compressed to start contacting with each other through the holes of air spacer, the capacitance increased instantly as

the ionic transportation occurred. It is worth to mention that the thickness, modulus of the spacer played an important role in the sensing performance (more information can be found in Figs. S12 and S13 [26]). We therefore used the soft silicone with 500 μm as the spacer to set the pressure threshold (444.4 Pa in this study). Additionally, the microstructure and drying state of the ionic film also very important as shown in Figs. S14–S16. Once the contacting started, the sensor still has a lot of room to increase capacitance under added pressure, resulting from the low contact surface area at the beginning and rough surface (duplicating from the abrasive paper) of the membrane. Further adding pressure would promote an intimate contact of the upper/bottom electrode with the membrane and thus lead to an ultrahigh capacitance due to the $\text{Ti}_3\text{C}_2\text{T}_x$ -induced intercalating behaviors. The $\text{Ti}_3\text{C}_2\text{T}_x$ -induced ultrahigh pseudocapacitance, compare to the typical EDL capacitance, results

in the high capacitance variation. However, considered that the mechanical property of the substrate materials used, the sensing range therefore is determined to be 1.4 MPa (Fig. S7). Throughout the process, the flexible yet mechanically robust n-WF with constructed intertwined structure provided an electrode substrate with largely enhanced surface area, which contributes to the excellent electrochemical performance. Besides, the intertwined and porous layer is expected to prevent the restacking of flakes and facilitate ionic transport and access to $\text{Ti}_3\text{C}_2\text{T}_x$ nanosheets. Overall, the spacer determined a dominant role in the sensitivity, while the pseudocapacitance also made a great contribution, because of its significant decrease of the initial capacitance to increase the sensitivity. Such a rationally designed flexible pressure sensor with ultrahigh sensitivity and broader sensing range, using the MXene as the capacitive materials, opens a gate for more promising applications.

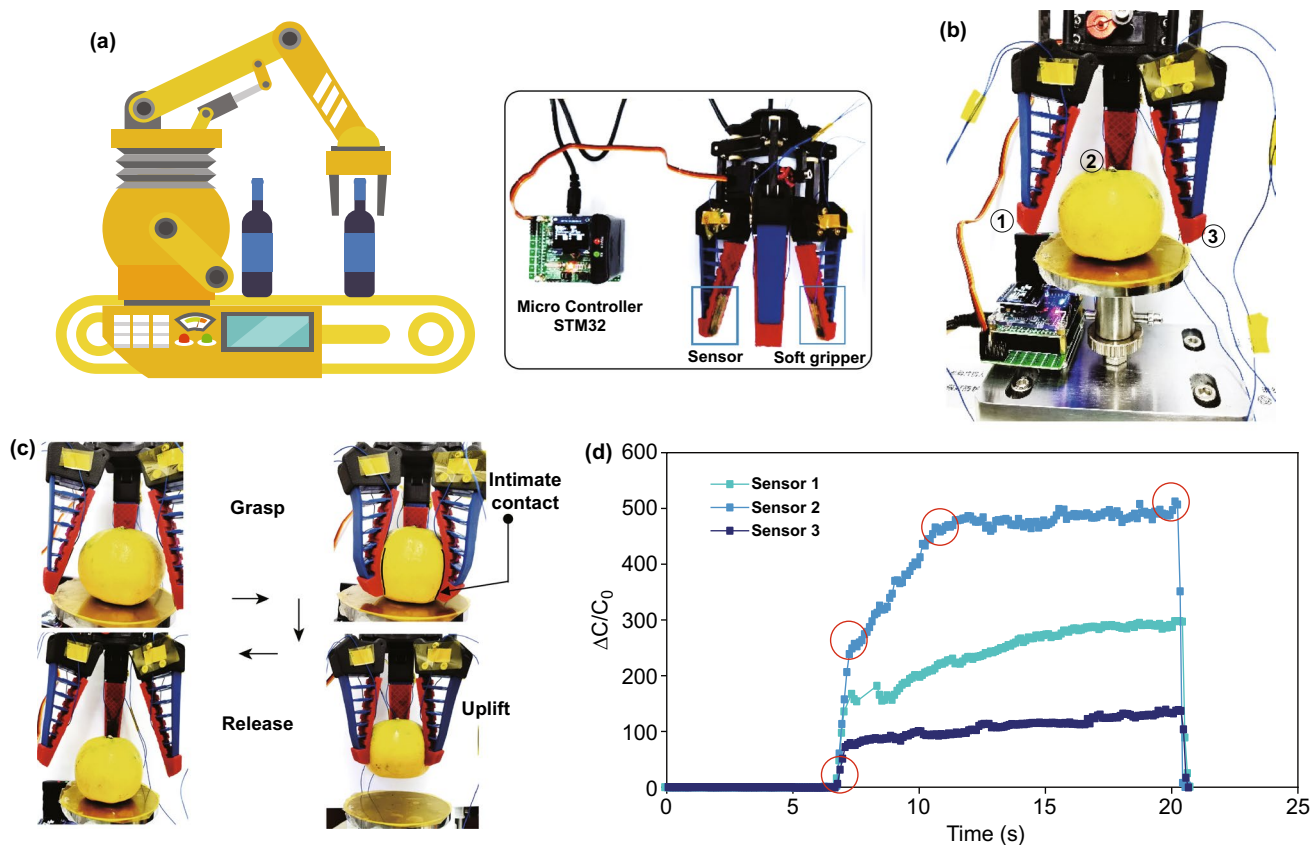


Fig. 6 Practical application of the flexible iontronic sensor for electronic skin. **a, b** Configuration of the wirelessly controlled soft gripper with flexible sensor to achieve product grasping. **c** Procedures for the soft gripper to capture and release the orange. **d** Capacitance variations of the sensor during the process to grasp and release the sample

3.3 Application of the Sensor

The practical applications of the sensor are shown in Fig. 5. Firstly, the sensing performance of our sensor was evaluated via detecting foot plantar pressure. The sensor was mounted inside the shoes, where high pressure forms during running or strenuous exercise caused by the rapid change of the acceleration (Fig. 5a). The activities of a human's standing, walking and running was successfully monitored (Fig. 5b). The fast Fourier transform (FFT) results indicate that both the intensity and frequency of the output signal for running state are larger than those of walking state (Fig. 5c). Data of the sensor for walking process of the sensor were collected to analyze the physical activity. It was clearly observed that the profiles remained a similar tendency (Fig. 5d). It was mainly composed of 4 processes. From the step I to step II, the pressure gradually increased during the compaction of the feet sole and the ground and then reached its maximum value upon the foot sole in full contact with the ground (III) and finally decreased to its original state I with the foot lifted (IV). Even for a long-term walking, the sensor can keep a reliable stability (Fig. S17). Additionally, we also tested the force resolution of the TIPS to monitor the bear load for a man (Body weight, 71 kg). During the test, the sensor mounted in a shoe is capable of accurately detecting the added load (one bag, 1 kg) for a man under walking state, demonstrating its potential application on a smart insole system [48]. The application of the sensor at low pressure was also investigated as shown in Fig. S18, which can successfully monitor the pulse rate and eyes blink. Even in a harsh environment, the sensor enabled to retain its original capacitance for a long-term durability (Fig. S19).

To further demonstrate its application as a tactile sensor, we directly installed the sensor on the surface of a customized soft gripper contacting with the grasped objects. The corresponding setup is shown in Fig. 6a. Since the traditional rigid grippers cannot directly capture the objects with irregular shapes or soft properties due to lack of conformality, a customized soft fin ray-like manipulator was designed and fabricated. The gripper was controlled to grasp an orange, and the corresponding grasping force was monitored by the sensor during this process (Fig. 6b, c). It can be seen that the soft gripper possessed perfect shape adaptability to fit the geometrical morphology of the orange and successfully moved it up. The force initially increased rapidly in grasping the orange, then slowly increased when lifting it

up, and finally reached a stable level to fully fix the orange. Once releasing the orange, the force decreased instantly to its initial value. Finally, a sensor array was practically demonstrated to recognize the geometric projection shape of various samples including flash disk and solid gum with a concave bottom, indicating its high resolution and large-scale manufacturing potential (Fig. S20).

4 Conclusion

In summary, $\text{Ti}_3\text{C}_2\text{T}_x$ is used as the pseudocapacitive electrode materials to fabricate the flexible iontronic sensor instead of the energy storage device for the first time. Due to the intercalation-induced high capacitance and rationally designed structural configuration, the sensor showed unprecedentedly ultrahigh sensitivity of over $46,730 \text{ kPa}^{-1}$ and incomparable broad sensing range of 1.4 MPa with long-term durability (no decay over 10,000 cycles) under high pressure. Specifically, the high-pressure results in an increase in the accessible surface area and shortened ions transportation pathway for the MXene-based sensor. Additionally, a facile laser-engraving was proved to be a fast methodology for the composite electrode, which can also be extended to fabricate other MXene-based composite structures in the future for flexible electronics. As practical demonstrations, the flexible sensor not only can precisely distinguish the exercise frequency and the intensity when monitoring the human activities with attached to the shoe sole, but also can be used as a pressure-sensing skin for measuring the grasping force of a soft robotic gripper. This study rationally exploited MXene's intercalation-induced pseudocapacitance for the iontronic pressure sensor beyond typically developing the MXene as energy storage materials or simply using its conductive feature as a piezoresistive sensor. We believe that our work will significantly broaden the research and application of the iontronic sensor through using the pseudocapacitive or even battery-type capacitive materials instead of the traditional EDL electrode. This work gives a concept guide for the experts to explore more potential in supercapacitor area.

Acknowledgements These authors would like to acknowledge the financial support of the project from the National Natural Science Foundation of China (No. 61904141), the funding of Natural Science Foundation of Shaanxi Province (No. 2020JQ-295), China Postdoctoral Science Foundation (2020M673340), the Fundamental Research Funds for the Central Universities (JB210407), the

Key Research and Development Program of Shaanxi (Program No. 2020GY-252; No. 2021GY-277) and National Key Laboratory of Science and Technology on Vacuum Technology and Physics (HTKJ2019KL510007).

Author contributions Libo Gao designed and fabricated samples, conducted experiments, analyzed data and wrote the manuscript. Meng Wang analyzed data, conducted experiments and drafted the manuscript partially. Hongcheng Xu wrote the manuscript partially and revised the manuscript. Ke Cao performed the SEM and TEM experiments. Libo Gao and Lei Li led this project. Other authors also contributed great help to this work. All authors have approved the better final version of the paper.

Open Access This article is licensed under a Creative Commons Attribution 4.0 International License, which permits use, sharing, adaptation, distribution and reproduction in any medium or format, as long as you give appropriate credit to the original author(s) and the source, provide a link to the Creative Commons licence, and indicate if changes were made. The images or other third party material in this article are included in the article's Creative Commons licence, unless indicated otherwise in a credit line to the material. If material is not included in the article's Creative Commons licence and your intended use is not permitted by statutory regulation or exceeds the permitted use, you will need to obtain permission directly from the copyright holder. To view a copy of this licence, visit <http://creativecommons.org/licenses/by/4.0/>.

Supplementary Information The online version contains supplementary material available at <https://doi.org/10.1007/s40820-021-00664-w>.

References

1. S. Sundaram, P. Kellnhofer, Y. Li, J.Y. Zhu, A. Torralba et al., Learning the signatures of the human grasp using a scalable tactile glove. *Nature* **569**, 698–702 (2019). <https://doi.org/10.1038/s41586-019-1234-z>
2. M.K. Kim, C. Kantarcigil, B. Kim, R.K. Baruah, S. Maity et al., Flexible submental sensor patch with remote monitoring controls for management of oropharyngeal swallowing disorders. *Sci. Adv.* **5**, 1–10 (2019). <https://doi.org/10.1126/sciadv.aay3210>
3. B. Shih, D. Shah, J. Li, T.G. Thuruthel, Y.-L. Park et al., Electronic skins and machine learning for intelligent soft robots. *Sci. Robot* (2020). <https://doi.org/10.1126/scirobotics.aaz9239>
4. W. Fan, Q. He, K. Meng, X. Tan, Z. Zhou et al., Machine-knitted washable sensor array textile for precise epidermal physiological signal monitoring. *Sci. Adv.* **6**, 1–11 (2020). <https://doi.org/10.1126/sciadv.aay2840>
5. S. Mishra, Y.S. Kim, J. Intarasirisawat, Y.T. Kwon, Y. Lee et al., Soft, wireless periocular wearable electronics for real-time detection of eye vergence in a virtual reality toward mobile eye therapies. *Sci. Adv.* **6**, 1–12 (2020). <https://doi.org/10.1126/sciadv.aay1729>
6. Y. Yu, J. Nassar, C. Xu, J. Min, Y. Yang et al., Biofuel-powered soft electronic skin with multiplexed and wireless sensing for human-machine interfaces. *Sci. Robot* (2020). <https://doi.org/10.1126/scirobotics.aaz7946>
7. X. Yu, Z. Xie, Y. Yu, J. Lee, A. Vazquez-Guardado et al., Skin-integrated wireless haptic interfaces for virtual and augmented reality. *Nature* **575**, 473–479 (2019). <https://doi.org/10.1038/s41586-019-1687-0>
8. Y. Yang, Y. Song, X. Bo, J. Min, O.S. Pak et al., A laser-engraved wearable sensor for sensitive detection of uric acid and tyrosine in sweat. *Nat. Biotechnol.* **8**, 217–224 (2020). <https://doi.org/10.1038/s41587-019-0321-x>
9. K. Wang, Z. Lou, L. Wang, L. Zhao, S. Zhao et al., Bioinspired interlocked structure-induced high deformability for two-dimensional titanium carbide (MXene)/natural microcapsule-based flexible pressure sensors. *ACS Nano* **13**, 9139–9147 (2020). <https://doi.org/10.1021/acsnano.9b03454>
10. C. Zhang, W. Bin Ye, K. Zhou, H.Y. Chen, J.Q. Yang et al., Bioinspired artificial sensory nerve based on nafion memristor. *Adv. Funct. Mater.* (2019). <https://doi.org/10.1002/adfm.201808783>
11. C.M. Boutry, M. Negre, M. Jorda, O. Vardoulis, A. Chortos et al., A hierarchically patterned, bioinspired e-skin able to detect the direction of applied pressure for robotics. *Sci. Robot* (2018). <https://doi.org/10.1126/scirobotics.aau6914>
12. X. Tian, P.M. Lee, Y.J. Tan, T.L.Y. Wu, H. Yao et al., Wireless body sensor networks based on metamaterial textiles. *Nat. Electron.* **2**, 243–251 (2019). <https://doi.org/10.1038/s41928-019-0257-7>
13. Y.C. Huang, Y. Liu, C. Ma, H.C. Cheng, Q. He et al., Sensitive pressure sensors based on conductive microstructured air-gap gates and two-dimensional semiconductor transistors. *Nat. Electron.* **3**, 59–69 (2020). <https://doi.org/10.1038/s41928-019-0356-5>
14. Z. Wang, P. Li, R. Song, W. Qian, H. Zhou et al., High conductive graphene assembled films with porous micro-structure for freestanding and ultra-low power strain sensors. *Sci. Bull.* (2020). <https://doi.org/10.1016/j.scib.2020.05.002>
15. J.A. Rogers, T. Someya, Y. Huang, Materials and mechanics for stretchable electronics. *Science* **327**, 1603–1608 (2010). <https://doi.org/10.1126/science.1182383>
16. C. Wang, C. Wang, Z. Huang, S. Xu, Materials and structures toward soft electronics. *Adv. Mater.* **30**, 1–49 (2018). <https://doi.org/10.1002/adma.201801368>
17. S.T. Han, H. Peng, Q. Sun, S. Venkatesh, K.S. Chung et al., An overview of the development of flexible sensors. *Adv. Mater.* **29**, 1–22 (2017). <https://doi.org/10.1002/adma.201700375>
18. R. Shi, Z. Lou, S. Chen, G. Shen, Flexible and transparent capacitive pressure sensor with patterned microstructured composite rubber dielectric for wearable touch keyboard application. *Sci. China Mater.* **61**, 1587–1595 (2018). <https://doi.org/10.1007/s40843-018-9267-3>

19. K. Keum, J. Eom, J.H. Lee, J.S. Heo, S.K. Park et al., Fully-integrated wearable pressure sensor array enabled by highly sensitive textile-based capacitive ionotronic devices. *Nano Energy* **79**, 101631 (2021). <https://doi.org/10.1016/j.nanoen.2020.105479>
20. J.S. Kim, S.C. Lee, J. Hwang, E. Lee, K. Cho et al., Enhanced sensitivity of iontronic graphene tactile sensors facilitated by spreading of ionic liquid pinned on graphene grid. *Adv. Funct. Mater.* **30**, 1908993 (2020). <https://doi.org/10.1002/adfm.201908993>
21. A. Chhetry, J. Kim, H. Yoon, J.Y. Park, Ultrasensitive interfacial capacitive pressure sensor based on a randomly distributed microstructured iontronic film for wearable applications. *ACS Appl. Mater. Interfaces* **11**, 3438–3449 (2019). <https://doi.org/10.1021/acsami.8b17765>
22. R. Li, Q. Zhou, Y. Bi, S. Cao, X. Xia et al., Research progress of flexible capacitive pressure sensor for sensitivity enhancement approaches. *Sens. Actuators A Phys.* **321**, 112425 (2021). <https://doi.org/10.1016/j.sna.2020.112425>
23. N. Bai, L. Wang, Q. Wang, J. Deng, Y. Wang et al., Graded intrafillable architecture-based iontronic pressure sensor with ultra-broad-range high sensitivity. *Nat. Commun.* **11**, 3–11 (2020). <https://doi.org/10.1038/s41467-019-14054-9>
24. Y. Chang, L. Wang, R. Li, Z. Zhang, Q. Wang et al., First decade of interfacial iontronic sensing: from droplet sensors to artificial skins. *Adv. Mater.* **33**, 2003464 (2021). <https://doi.org/10.1002/adma.202003464>
25. B. Nie, R. Li, J.D. Brandt, T. Pan, Iontronic microdroplet array for flexible ultrasensitive tactile sensing. *Lab Chip* **14**, 1107–1116 (2014). <https://doi.org/10.1039/c3lc50994j>
26. Z. Zhu, R. Li, T. Pan, Imperceptible epidermal–iontronic interface for wearable sensing. *Adv. Mater.* **30**, 1–9 (2018). <https://doi.org/10.1002/adma.201705122>
27. J. Wang, S. Dong, B. Ding, Y. Wang, X. Hao et al., Pseudocapacitive materials for electrochemical capacitors: from rational synthesis to capacitance optimization. *Nat. Sci. Rev.* **4**, 71–90 (2017). <https://doi.org/10.1093/nsr/nww072>
28. M. Alhabeb, K. Maleski, B. Anasori, P. Lelyukh, L. Clark et al., Guidelines for synthesis and processing of two-dimensional titanium carbide ($\text{Ti}_3\text{C}_2\text{T}_x$ MXene). *Chem. Mater.* **29**, 7633–7644 (2017). <https://doi.org/10.1021/acs.chemmater.7b02847>
29. L. Gao, J. Song, J.U. Surjadi, K. Cao, Y. Han et al., Graphene-bridged multifunctional flexible fiber supercapacitor with high energy density. *ACS Appl. Mater. Interfaces* **10**, 28597–28607 (2018). <https://doi.org/10.1021/acsami.8b08680>
30. L. Gao, J.U. Surjadi, K. Cao, H. Zhang, P. Li et al., Flexible fiber-shaped supercapacitor based on nickel-cobalt double hydroxide and pen ink electrodes on metallized carbon fiber. *ACS Appl. Mater. Interfaces* **9**, 5409–5418 (2017). <https://doi.org/10.1021/acsami.6b16101>
31. M. Naguib, M. Kurtoglu, V. Presser, J. Lu, J. Niu et al., Two-dimensional nanocrystals produced by exfoliation of Ti_3AlC_2 . *Adv. Mater.* **23**, 4248–4253 (2011). <https://doi.org/10.1002/adma.201102306>
32. Y.Z. Zhang, Y. Wang, Q. Jiang, J.K. El-Demellawi, H. Kim et al., MXene printing and patterned coating for device applications. *Adv. Mater.* **32**, 1–26 (2020). <https://doi.org/10.1002/adma.201908486>
33. M.R. Lukatskaya, O. Mashtalir, C.E. Ren, Y. Dall’Agnese, P. Rozier et al., Cation intercalation and high volumetric capacitance of two-dimensional titanium carbide. *Science* **341**, 1502–1505 (2013). <https://doi.org/10.1126/science.1241488>
34. S.R.A. Ruth, V.R. Feig, H. Tran, Z. Bao, Microengineering pressure sensor active layers for improved performance. *Adv. Funct. Mater.* **30**, 2003491 (2020). <https://doi.org/10.1002/adfm.202003491>
35. L.X. Liu, W. Chen, H. Bin Zhang, Q.W. Wang, F. Guan et al., Flexible and multifunctional silk textiles with biomimetic leaf-like mxene/silver nanowire nanostructures for electromagnetic interference shielding, humidity monitoring, and self-derived hydrophobicity. *Adv. Funct. Mater.* **29**, 1–10 (2019). <https://doi.org/10.1002/adfm.201905197>
36. A. Ren, J. Zou, H. Lai, Y. Huang, L. Yuan et al., Direct laser-patterned MXene-perovskite image sensor arrays for visible-near infrared photodetection. *Mater. Horizons* **7**, 1901–1911 (2020). <https://doi.org/10.1039/d0mh00537a>
37. Q. Li, R. Yin, D. Zhang, H. Liu, X. Chen et al., Flexible conductive MXene/cellulose nanocrystal coated nonwoven fabrics for tunable wearable strain/pressure sensors. *J. Mater. Chem. A* **8**, 21131–21141 (2020). <https://doi.org/10.1039/d0ta07832h>
38. B. Lee, J.Y. Oh, H. Cho, C.W. Joo, H. Yoon et al., Ultraflexible and transparent electroluminescent skin for real-time and super-resolution imaging of pressure distribution. *Nat. Commun.* **11**, 1–11 (2020). <https://doi.org/10.1038/s41467-020-14485-9>
39. C. Wu, T. Zhang, J. Zhang, J. Huang, X. Tang et al., A new approach for an ultrasensitive tactile sensor covering an ultrawide pressure range based on the hierarchical pressure-peak effect. *Nanoscale Horizons* **5**, 541–552 (2020). <https://doi.org/10.1039/c9nh00671k>
40. M. Chen, X. Hu, K. Li, J. Sun, Z. Liu et al., Self-assembly of dendritic-lamellar MXene/Carbon nanotube conductive film for wearable tactile sensors and artificial skin. *Carbon* **164**, 111–120 (2020). <https://doi.org/10.1016/j.carbon.2020.03.042>
41. L. Zhang, X. Liu, M. Zhong, Y. Zhou, Y. Wang et al., Micro-nano hybrid-structured conductive film with ultrawide range pressure-sensitivity and bioelectrical acquirability for ubiquitous wearable applications. *Appl. Mater. Today* **20**, 100651 (2020). <https://doi.org/10.1016/j.apmt.2020.100651>
42. X. Tang, C. Wu, L. Gan, T. Zhang, T. Zhou et al., Multilevel microstructured flexible pressure sensors with ultrahigh sensitivity and ultrawide pressure range for versatile electronic skins. *Small* **15**, 1–9 (2019). <https://doi.org/10.1002/sml.201804559>
43. Z. Xiao, W. Zhou, N. Zhang, Q. Zhang, X. Xia et al., All-carbon pressure sensors with high performance and excellent chemical resistance. *Small* **15**, 1–7 (2019). <https://doi.org/10.1002/sml.201804779>
44. Y. Lee, J. Park, S. Cho, Y.E. Shin, H. Lee et al., Flexible ferroelectric sensors with ultrahigh pressure sensitivity and linear response over exceptionally broad pressure range. *ACS Nano* **12**, 4045–4054 (2018). <https://doi.org/10.1021/acsnano.8b01805>



45. B. Feng, G. Zou, W. Wang, M. Dong, Y. Xiao et al., A programmable, gradient-composition strategy producing synergistic and ultrahigh sensitivity amplification for flexible pressure sensing. *Nano Energy* **74**, 104847 (2020). <https://doi.org/10.1016/j.nanoen.2020.104847>
46. S. Xu, G. Wei, J. Li, W. Han, Y. Gogotsi, Flexible MXene-graphene electrodes with high volumetric capacitance for integrated co-cathode energy conversion/storage devices. *J. Mater. Chem. A* **5**, 17442–17451 (2017). <https://doi.org/10.1039/c7ta05721k>
47. S. Xu, Y. Dall’Agnese, G. Wei, C. Zhang, Y. Gogotsi et al., Screen-printable microscale hybrid device based on MXene and layered double hydroxide electrodes for powering force sensors. *Nano Energy* **50**, 479–488 (2018). <https://doi.org/10.1016/j.nanoen.2018.05.064>
48. J. Tao, M. Dong, L. Li, C. Wang, J. Li et al., Real-time pressure mapping smart insole system based on a controllable vertical pore dielectric layer. *Microsystems Nanoeng.* **6**, 1–10 (2020). <https://doi.org/10.1038/s41378-020-0171-1>